Use of Surface Photovoltage Spectroscopy to Probe Energy Levels and Charge Carrier Dynamics in Transition Metal (Ni, Cu, Fe, Mn, Rh) Doped $SrTiO_3$ Photocatalysts for H_2 Evolution from Water

Journal:	*Journal of Materials Chemistry A*
Manuscript ID	TA-ART-12-2017-010934.R1
Article Type:	Paper
Date Submitted by the Author:	10-Feb-2018
Complete List of Authors:	Ma, Xiaoqing; Fudan University, Cui, Xiaoli; Fudan University, Zhao, Zeqiong; University of California, Department of Chemistry Alves Melo Jr, Mauricio; University of California, Davis, Chemistry Department Roberts, Emily; University of Southern California, Chemistry Osterloh, Frank ; University of California, Department of Chemistry

Journal Name

ARTICLE

Use of Surface Photovoltage Spectroscopy to Probe Energy Levels and Charge Carrier Dynamics in Transition Metal (Ni, Cu, Fe, Mn, Rh) Doped $SrTiO_3$ Photocatalysts for H_2 Evolution from Water

Received 00th January 20xx,
Accepted 00th January 20xx

DOI: 10.1039/x0xx00000x

www.rsc.org/

Xiaoqing Ma,[a,b] Xiaoli Cui,[a] Zeqiong Zhao,[b] Mauricio A. Melo Jr.,[b] Emily J. Roberts,[c] and Frank E. Osterloh*[b]

Doping with transition metal ions is widely employed to adjust the optical and photocatalytic properties of wide band semiconductors, however, quantitative information about the energetics and charge transfer dynamics of the impurity states is often difficult to obtain. Here we use surface photovoltage spectroscopy (SPS), optical spectroscopy, and irradiation experiments to study the effect of several dopants on the ability of $SrTiO_3$ nanocrystals to generate a photovoltage and to catalyse H_2 evolution from aqueous methanol. Phase pure $SrTiO_3$:TM nanocrystals with TM=Ni, Cu, Fe, Mn, Rh were synthesized by hydrothermal reaction of TiO_2, $Sr(OH)_2$, KOH, and transition metal chlorides and nitrates in water. SPS data was obtained on thin films of these nanocrystals on fluorine doped tin oxide substrates under vacuum atmosphere. All samples are n-type, which can be gauged from the negative photovoltage caused by the transfer of electrons into the FTO substrate. All dopants produce sub-bandgap states in the $SrTiO_3$ lattice, whose energetic positions can be determined from the photovoltage onset energy in SPS and from optical absorption spectra. The reversibility and size of the photovoltage provide information about the photohole dynamics and their ability to oxidize sacrificial electron donors at the nanocrystal surface. Overall, this work provides an explanation for the inability of Ni, Cu, Fe, Mn dopants to enhance visible light photocatalytic activity in $SrTiO_3$, and it establishes SPS as a useful tool to map the energetics and photochemistry of impurity states in metal oxide nanocrystals.

Introduction

Photocatalytic water splitting is a promising approach for the generation of carbon free fuel via conversion of sunlight.[2, 3] Because of its high stability and suitable band edge positions, $SrTiO_3$ has been studied as a photocatalyst for the water splitting reaction. Its main disadvantage is its large band gap of 3.2 eV that makes it suitable to only absorb photons in the ultraviolet region of the spectrum.[4, 5] This limit can be potentially overcome through introduction of foreign elements that generate visible light absorbing sub-gap states.[6, 7] In the ABO_3 perovskite structure type, dopants can occupy both A and B sites,[8] allowing great flexibility for doping. However, of the many transition metals (Ag and Pb,[9] La, Nb, Ta and Ni,[10-12]Cr,[13-16] Ir,[6] Mn,[17, 18] Ru, Pd, Pt and Rh,[19-21] Sb,[22] Fe,[18, 23] and Cu[24], V, Mo, W,[25] and Co [18]) that have been incorporated into the $SrTiO_3$ lattice, only some, such as Rh, [1, 19, 26, 27] actually improve the photocatalytic activity in the visible region. The majority of ions decrease the photocatalytic activity because the partially filled d-orbitals of transition metals dopants capture both electrons and holes and act as recombination centers.[28] Also, when the dopant valence differs from that of Ti^{4+}, oxygen vacancies and Ti^{3+} states are often formed as a result of charge compensation. These additional defect states can also act as recombination sites. [17, 23, 29, 30] Overall, the understanding of the structure, energetics, and dynamics of the transition metal dopants in $SrTiO_3$ and other metal oxides is central to solar energy conversion and photocatalytic applications with such materials. However, experimental information about the energetics and redox properties of the dopants is very difficult to obtain.[18, 20, 31, 32] Herein, we apply surface photovoltage spectroscopy (SPS) to observe the photochemistry of transition metal doped $SrTiO_3$:TM nanocrystals (TM =Ni, Cu, Fe, Mn and Rh). In SPS the photovoltage of an illuminated particle film is measured in a contactless way under vacuum conditions with a semi-transparent Kelvin probe. [33] The photovoltage corresponds to movement of photogenerated charge carriers in the particle film or its interfaces. It provides information about the majority carrier type and effective band gap, [34] built-in potential, [35] carrier trapping, [36] recombination, [37] and redox reactions of the sample.[1] In contrast to photoelectrochemistry, photovoltages acquired by SPS do not require any Faradaic

[a] *Department of Materials Science, Fudan University, Shanghai, 200433, P.R.China.*
[b] *Department of Chemistry, University of California, Davis. One Shields Avenue, Davis, CA, 95616, USA. Fax: (+1)530 752 8995; E-mail: fosterloh@ucdavis.edu.*
[c] *Department of Chemistry, 840 Downey Way, University of Southern California, Los Angeles, California 90089-0744, United States.*

Electronic supplementary information (ESI) available: XRD patterns, XPS data, photovoltage data and spectra, hydrogen evolution data, optical data, and elemental analysis results. See DOI: 10.1039/xxxxxx.

process to occur at the nanocrystal surface. That makes it possible to observe the intrinsic photochemistry of the samples. Also, the technique is at least three orders of magnitude more sensitive than photoelectrochemistry. [38] As shown below, TM doped $SrTiO_3$ nanocrystals produce strong sub-bandgap photovoltage signals that arise from the impurity states. By comparing the photoonset potentials with the optical spectra, it becomes possible to estimate the energy positions of the dopants in the lattice. Additionally, reversibility and size of the photovoltage in the presence and absence of methanol provide information about the reactivity of the photoholes. It is found that only $Rh:SrTiO_3$ can generate reactive and mobile photoholes, which explains the superior visible light H_2 evolution activity of Rh-doped $SrTiO_3$ nanocrystals. In contrast, Ni, Cu, Fe, Mn doped $SrTiO_3$ nanocrystals are found to generate weak and irreversible photovoltage under visible excitation, which agrees with their low photocatalytic H_2 evolution activity. These results confirm that SPS is a useful tool for the identification of dopants in $SrTiO_3$, for mapping their energetics, and for probing their redox behaviour.

Results and Discussion

Fig.1 shows a summary of XRD patterns for as synthesized $SrTiO_3$ and TM (Ni, Cu, Fe, Mn, Rh) doped $SrTiO_3$ nanocrystals. All diffraction peaks can be assigned to the cubic perovskite structure type and there are no discernible impurities. Based on the Scherrer equation, the average crystallite size is 35 nm.[39] Incorporation of the metal ions was verified by X-ray Fluorescence spectroscopy (Table S1). Accordingly, Ni, Cu, Fe, Mn, Rh ions are present at 0.44, 1.24, 1.70, 1.73, 1.05 mol% respectively in these samples. Based on their size, the TM (Ni, Cu, Fe, Mn, Rh) ions most likely occupy the Ti^{4+} site in the $SrTiO_3$ lattice (Table S2). Insertion of the TM ions into lattice is also revealed by shifts of the (110) peak in the XRD patterns (Fig.S1). A shift to larger diffraction angle (smaller unit cell) is observed on $Mn:SrTiO_3$ which agrees with the smaller ion radii of Mn^{3+} and Mn^{4+} compared to Ti^{4+} (Table S2). The same is found for the Ni-doped sample. In contrast, $Rh:SrTiO_3$ exhibits a shift of the (110) peak to smaller angle (large unit cell), in agreement with the larger size of Rh^{3+}, compared to Ti^{4+}. No change is observed for Cu and Fe doped samples. XPS spectra of the doped $SrTiO_3$ nanocrystals were attempted to obtain information about the valence of the TM ions. Apart from Rh, no signals for the dopants were detected because of their low concentration. To avoid this problem, a second set of TM doped nanocrystals was synthesized by doubling the concentrations of the dopants. XPS spectra for this set of materials are shown in Figure S2. The spectra support the presence of nickel as Ni^{3+} with a small contribution of Ni^{2+}. Iron is present in the Fe^{2+} state with smaller contributions from Fe^{3+} and Fe^{4+}. Manganese is found as Mn^{2+} with some Mn^{3+} and Mn^{4+} present also. Rhodium is found as Rh^{3+} exclusively when 6 mol% of $RhCl_3$ was present during the synthesis, but some Rh^{4+} is detected in the samples synthesized with 3 mol% $RhCl_3$ present. Copper was below the detection limit. Analysis of the Titanium $2p_{1/2}$ and $2p_{3/2}$ signals showed the expected +4 oxidation state exclusively, but revealed small Ti^{3+} populations for the Rh and Cu-doped $SrTiO_3$ samples.

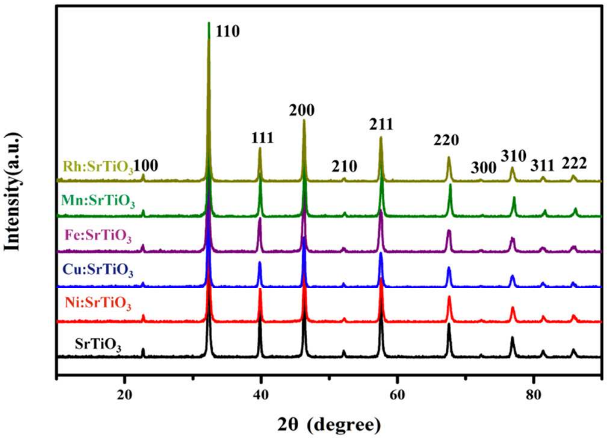

Figure 1. XRD patterns of as-prepared $SrTiO_3$ and TM (Ni, Cu, Fe, Mn, Rh) doped $SrTiO_3$ nanoparticles.

Figure 2 displays the TEM images and corresponding size distribution histograms for doped and non-doped $SrTiO_3$ nanocrystals. Most nanocrystals have a cubic morphology with edge lengths of 34±9.3, 35±6.4, 39±6.5, 36±6.6, 38±6.6 and 39±9.0 nm, for samples shown in 2A-F, respectively.

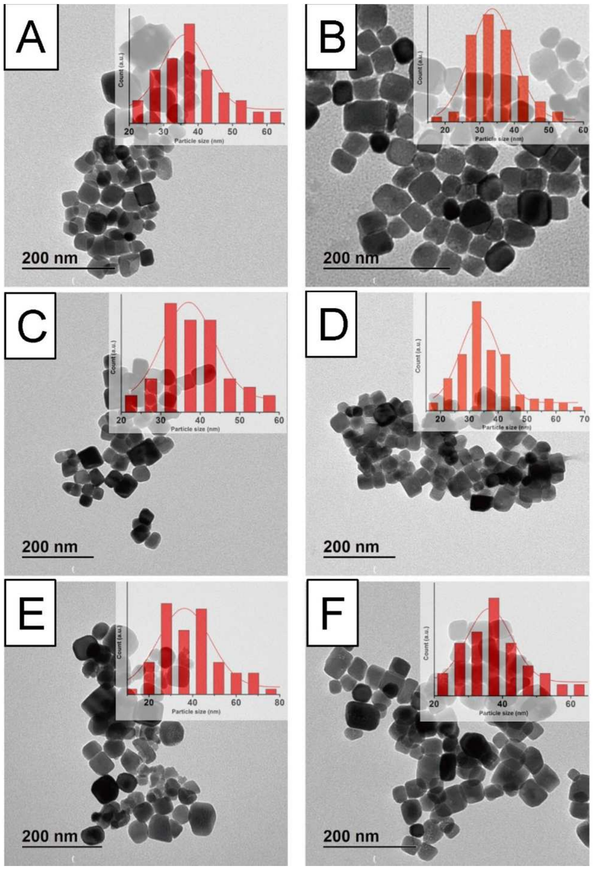

Figure 2. TEM images with size statistics (inset) of $Ni:SrTiO_3$ (A), $Cu:SrTiO_3$ (B), $Fe:SrTiO_3$ (C), $Mn:SrTiO_3$ (D), $Rh:SrTiO_3$ (E), and $SrTiO_3$ (F).

This indicates that the introduction of the transition metal ions does not affect crystal growth. Also, the match between TEM diameter and Scherrer particles size suggests that most particles are single crystals. This is confirmed by high resolution TEM and selected area diffraction data for Ni-doped $SrTiO_3$ (Fig. S3).

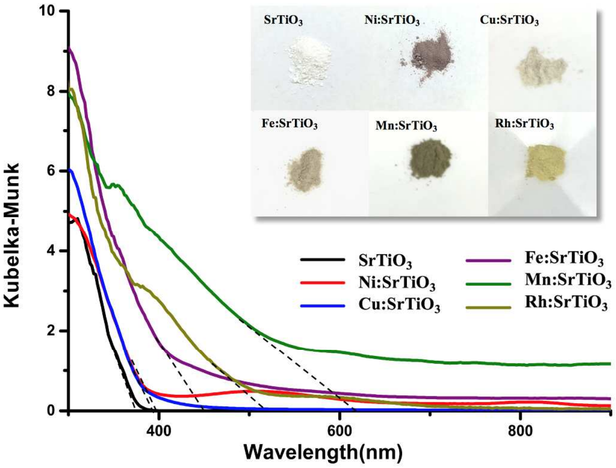

Figure 3. UV-vis absorption spectra and photos of TM (Ni, Cu, Fe, Mn, Rh) doped and undoped $SrTiO_3$ nanoparticles.

Photographs of the samples are depicted in Fig.3 along with diffuse reflectance absorption spectra (DRS). Non-doped $SrTiO_3$ is plain white and exhibits an absorption edge at 385 nm, in agreement with its 3.2 eV band gap. The addition of nickel gives the Ni:$SrTiO_3$ sample a pink appearance and leads to a broad absorption band at 520 nm, which is assigned to a d−d transition of Ni^{3+} cations.[40] The Cu:$SrTiO_3$ appears off-white and exhibits an absorption onset shifted to 400 nm (3.1 eV) which is assigned to the transition from Cu 3d electrons to the $SrTiO_3$ conduction band. These and other optical data are listed in Table S2. Iron and Mn doped samples appear grey and green-gray. Their optical spectra show absorption edges strongly shifted into the visible plus a long absorption tail that extends beyond 800 nm. The shift in absorption edge suggests that optical excitation of metal 3d electrons into the conduction band of the host is possible. The absorption tail is attributed to the variation of dopant oxidation states as suggested by the XPS data. Lastly, Rh-doped $SrTiO_3$ is yellow and has an absorption onset of 510 nm (2.3 eV) arising from excitation of Rh^{3+} d-electrons into the titanate conduction band. The tail reaching to 700 nm is due to residual Rh^{4+}. [41]

Surface photovoltage spectra (SPS) were recorded on thin films of the TM (Ni, Cu, Fe, Mn, Rh):$SrTiO_3$ nanocrystals on fluorine doped tin oxide substrates. These spectra are shown in Fig. 4 together with diffuse reflectance absorption spectra of each sample. All spectra show negative photovoltage signals that are typically associated with the transfer of electrons to the FTO substrate. This shows that all samples are n-type. For non-doped $SrTiO_3$, the photovoltage onset at 3.1 eV closely matches the absorption edge of the material (3.2 eV). For all TM doped STO films, the photoonset energies are shifted into the visible region, similar to what was seen in the optical spectra of these compounds (onset values are listed in Table S2). For Fe- and Rh-doped $SrTiO_3$, the photovoltage onset agrees well with the optical absorption edges, while for Ni-doped $SrTiO_3$, the photovoltage onset at 2.75 eV is below the absorption onset (3.1 eV) and 0.35 eV shifted above the Ni d-d transition peak (2.4 eV). This suggests that charge carriers generated at 2.4 eV excitation are not mobile (see further discussion below). A similar situation exists for Mn:$SrTiO_3$, where the photovoltage onset at 2.45 eV is found above the energy of the optical absorption edge (2.0 eV). In contrast, for Cu:$SrTiO_3$ the photovoltage onset at 2.7 eV is shifted to lower energy compared to the absorption edge of this material (3.1 eV). Apparently, the states involved in the weak absorption tail seen in Fig. 3 can contribute mobile electrons under excitation.

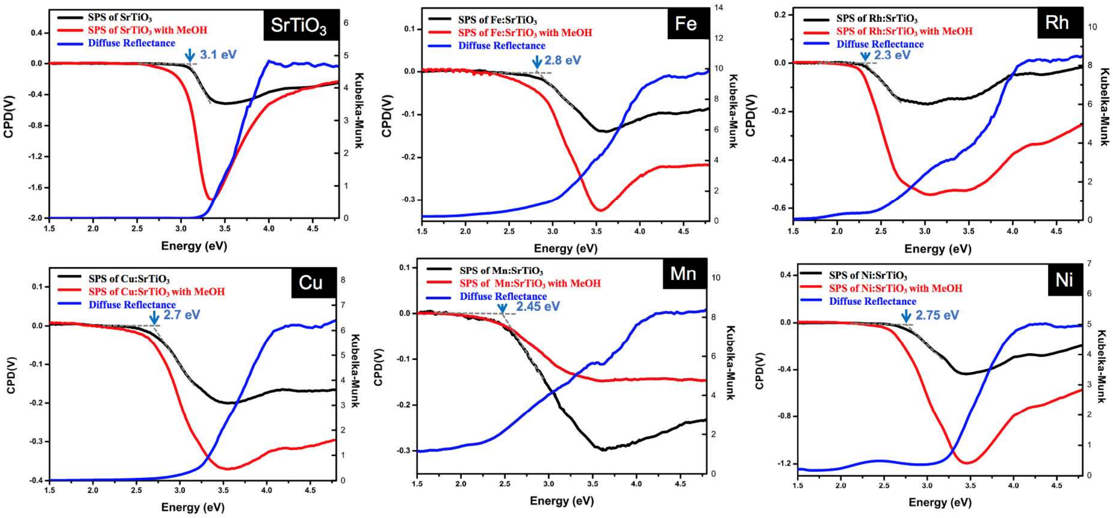

Figure 4. SPS (black and red) and diffuse reflectance (blue) spectra of TM (Ni, Cu, Fe, Mn, Rh) doped and undoped $SrTiO_3$ on FTO substrates. Red traces show photovoltage spectra after exposing the films to methanol. Above 3.5 eV, the photovoltage is limited by the light penetration depth of the sample and the diminished light intensity of the light source (for spectrum see reference [1]).

Lastly, for Rh:$SrTiO_3$, it is noted that the small optical absorption peak at 2.0 eV does not produce a photovoltage signal. This peak is attributed to photochemically non-active Rh^{4+} species, as discussed above. Additional differences between the TM-doped $SrTiO_3$ nanocrystals become visible by comparing the relative sizes of photovoltage signals under visible and UV illumination, Fig. 4). While Ni, Cu, Fe, Mn and non-doped $SrTiO_3$ reach their maximum photovoltage signal only under UV excitation of the $SrTiO_3$ host (at 3.5 eV), the Rh-doped sample achieves its maximum voltage signal already under 3.0 eV illumination. This indicates that the Rh^{3+} dopants are more effective than the other TM ions at promoting charge separation in this material. This may be attributed to the greater reversibility of the $Rh^{4+/3+}$ redox couple [42] and the larger size of the Rh-d orbitals which promotes better overlap with the lattice ions.

In order to probe the ability of the photoexcited TM states to oxidize molecular adsorbates, SPS scans were recorded after exposing the films to a few drops of the sacrificial electron donor methanol (Fig. 4 and S4 and Table S3). Previous SPS studies on Rh:$SrTiO_3$ revealed that photochemical oxidation of sacrificial electron donors (iodide, methanol) can be observed as a photovoltage boost.[1] As can be seen from the red traces in Fig. 4, the addition of methanol causes a photovoltage increase in most samples and a shift of the photoonset to lower energy values. This indicates that mid-bandgap states are able to promote methanol oxidation upon excitation. For non-doped $SrTiO_3$ methanol causes a 0.25 V photovoltage increase at 3.0 eV and a 1.25 V photovoltage increase at 3.5 eV. This is in agreement with a previous report of defect-induced visible light H_2 evolution from $SrTiO_3$.[43] Samples of Cu, Fe-doped $SrTiO_3$ also produce significant photovoltage increases at 3.5 eV illumination, however, the boost at 3.0 eV is comparable or less than what is found for non-doped $SrTiO_3$ (Table S3 and Fig. S4). This suggests that the states responsible for the methanol oxidation are associated with the $SrTiO_3$ host and not with the Cu and Fe dopants. The situation is markedly different for Rh:$SrTiO_3$ which achieves its maximum photovoltage under 3.0 eV excitation. This suggests that photoholes generated on the Rh(3+) sites are able to reach the adsorbed methanol on the nanocrystal surface. As the only sample, Mn:$SrTiO_3$ shows a photovoltage reduction at both 3.0 and 3.5 eV when treated with methanol. This behavior is difficult to explain without further experiments. A possible reason is that methanol treatment produces Mn states that promote electron hole recombination in the catalyst. Lastly, Ni:$SrTiO_3$ shows a 0.4 V photovoltage boost at 3.0 illumination and a 0.7 V boost at 3.5 eV. This shows that Ni contributes states that can photooxidize methanol under visible excitation, similar to Rh.

Next, in order to probe the charge transfer dynamics of the transition metal doped nanocrystals, time-dependent photovoltage traces were recorded using light on-off cycles under visible and UV illumination, respectively. Non-doped $SrTiO_3$ nanocrystals (Fig. 5A) were found to generate small reversible photovoltage (-0.01 to -0.03 V) under 2.7 eV excitation and large reversible photovoltage (-0.85 V) under band gap excitation (3.2 eV). The 2.7 eV states are likely associated with lattice and surface defects of the material.[43, 44] Photovoltage formation occurs on the 5-10 minute scale for visible and UV excitation respectively, while photovoltage decay occurs on the 2-5 min timescale. The slow timescale for photovoltage generation shows that charge carriers move by diffusion. The decay is faster because return of the charge carriers into the depleted nanocrystal film is assisted by the electric field at the nanocrystal-substrate interface. The visible light induced transient photovoltage for the Fe-doped $SrTiO_3$ nanocrystals (Fig. 5) is very similar to that of non-doped $SrTiO_3$, but differences arise in the UV region. Here the photovoltages are smaller, less reversible, and also the timescale is slower, especially for the photovoltage decay. This suggests that carriers are fewer in concentration and less mobile, and become trapped in Fe sub-gap states. It is well known that unpaired electrons in high spin $3d^5$ and $3d^4$ configurations contribute to electron hole recombination.[45, 46 17, 23] On this basis, Fe is not beneficial to the photochemistry of $SrTiO_3$.

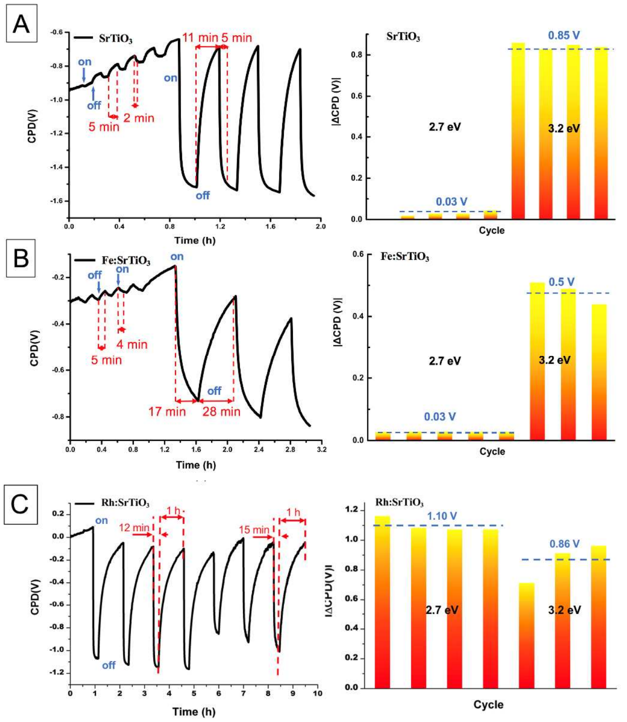

Figure 5. Transient photovoltage spectra of (A) non-doped $SrTiO_3$ on FTO substrate under intermittent illumination with a monochromatic light at 2.5 eV and 3.2 eV. (B) same for Fe:$SrTiO_3$ and (C) Rh:$SrTiO_3$. Data for all other samples is shown in Fig. S5.

Very similar behavior is seen for Mn-doped $SrTiO_3$ (Fig. S5), which is due to the ability of Mn^{3+} to trap both electrons and holes.[31] In contrast to the other samples, Rh:$SrTiO_3$ (Fig. 5C) exhibits large and reversible photovoltage formation under both 2.7 eV and 3.2 eV excitation. The average photovoltage under visible excitation (-1.10 V) exceeds that of the non-doped $SrTiO_3$ nanocrystal in the UV while the voltage under 3.2 eV excitation is about the same (-0.86 V). However, the timescales for photovoltage formation (12-15 mins) and decay (1 h) are much slower than for non-doped $SrTiO_3$. Charge transport in Rh:$SrTiO_3$ is slow because it involves hole hopping across the narrow $Rh^{4+/3+}$ impurity band.[42] Light-on/off cycles for the remaining samples are summarized in Fig. S5. The behavior of Cu:$SrTiO_3$ is similar to that of Fe-doped $SrTiO_3$, except this time, selective excitation of the Cu impurity states at 2.6 eV produces increasingly negative photovoltages, indicating gradual accumulation of photoholes in the sample, possibly at the Cu ion. Again, photovoltage generation under visible (22 min) and UV excitation (12 min) is slow. Irreversible oxidation of the dopant during multiply visible light excitation cycles can also be seen for Ni:$SrTiO_3$, as an increase of the photovoltage over time. This suggests the oxidized dopants (Ni^{3+}) may actually improve the photochemical properties of the material. However, the time periods required for the photovoltage formation (15 min) and recovery (45 min) remain slow under visible illumination.

In order to determine the effect of the metal dopants on photocatalytic H_2 evolution with $SrTiO_3$ under visible light, each sample was first modified with Pt (2.0 wt%) nanoparticles and then irradiated as an aqueous suspension with 20 vol% methanol as the hole scavenger. Figure 6 shows hydrogen evolution under 600 mW cm^{-2} visible illumination (>400 nm with longpass filter). All samples evolve H_2 under visible light illumination, but the amounts are too small to rule out a stoichiometric process. Only Rh:$SrTiO_3$-Pt evolves H_2 at higher rate, in agreement with earlier reports. [1, 21, 26] The activity of the Cu, Fe, Mn, and Ni-doped samples is comparable to non-doped $SrTiO_3$. The lack of visible light photocatalysis of the Cu, Fe, and Mn-doped nanocrystals is attributed to their inability to transport photoholes to the nanocrystal surface, based on the photovoltage data in Fig.4. For Ni-doped $SrTiO_3$, the SPS data in Fig. 4 confirmed that methanol could be oxidized, but the time dependent photovoltage measurement in Fig.S5 showed that charge transport is slow. This explains the low H_2 evolution activity in this case. Improved H_2 evolution activity can be achieved by increasing the amount of TM dopants during the synthesis of the samples (Table S4). Among that set of samples, Ni:$SrTiO_3$-Pt performed the best with 1.51 μmol h^{-1} H_2 and with an apparent quantum efficiency of 0.04% at 435 nm (Fig. S6). Using this value as a reference, the apparent quantum efficiency of the undoped and Ni, Cu, Fe, and Mn doped nanocrystals in Figure 6 can be estimated at 0.02% and that of the Rh doped $SrTiO_3$ nanocrystals as 0.71%.

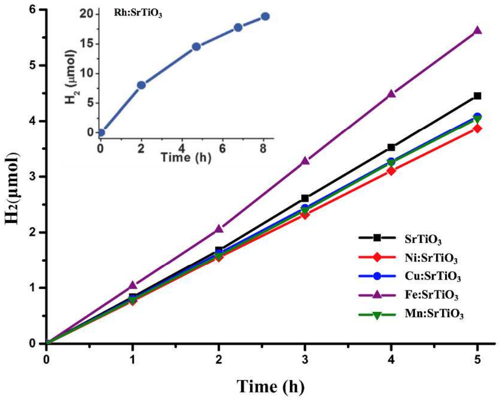

Figure 6. Hydrogen evolution from methanol solution containing Pt modified Ni, Cu, Fe, Mn: $SrTiO_3$ catalysts (50 mg in 50 mL of 20 vol% MeOH aqueous solution under light from Xe lamp at 600 mW cm^{-2} with > 400 nm long pass filter). Inset: H_2 evolution from 50 mg of Rh (3 mol%): $SrTiO_3$-Pt (2%) in 50 mL of 20 vol% MeOH aqueous solutions at pH 3.5 (adjusted with H_2SO_4). Under 112 mW cm^{-2} illumination with >400 nm longpass filter. [1]

Using the optical and photovoltage data in Fig. 3 and 4, we construct the energy diagram in Fig. 7 for the TM (Ni, Cu, Fe, Mn, Rh) doped samples. According to the scheme, the residual visible light activity of non-doped $SrTiO_3$ and the negative photovoltage at 3.1 eV are attributed to the excitation of oxygen vacancy defects (V_O) approximately 0.1 eV above the valence band. Excitation of these states produces mobile electrons in the $SrTiO_3$ conduction band and mobile holes in the oxygen defect band that can be used for the oxidation of methanol. The position of the V_O states agrees well with the results of photoelectron spectra of $SrTiO_3$ which place these states 0.15 eV above the valence band.[43] Introduction of Rh leads to Rh^{3+} t_{2g} states approximately 2.3 eV below the conduction band.[1] Excitation of these states produces a photovoltage that arises from electron movement through the $SrTiO_3$ conduction band into the FTO substrate. Photocatalysis and SPS confirm that the holes created in the Rh(3+) state can diffuse through the $SrTiO_3$ crystal and oxidize methanol. In contrast, Fe-ion produces states at 2.8 eV below E_{CB} that do not support hole transport. Instead photoholes become trapped at the Fe sites, turning them into recombination centers. The position of the Fe states near the valence band agrees well with earlier studies.[31, 32] Copper behaves similar to iron, with hole trap states forming 2.7 eV below the conduction band. A slightly different situation arises for Mn doped $SrTiO_3$. Here two sets of states are observed near the conduction and valence bands respectively. Transitions between these states are responsible for the 2.0 eV visible absorption of the material, and transitions from the Mn t_{2g} states to the conduction band are responsible for the 2.45 eV photovoltage onset in SPS. Based on SPS data in Figures 4 and 5, the Mn states do not produce mobile photoholes and act as electron-hole recombination sites instead. Nickel produces also two sets of energy states, but their effect on electron-hole recombination is less than for Mn. Photoholes from Ni can oxidize methanol, but their mobility is small to enable catalytic hydrogen production from aqueous methanol.

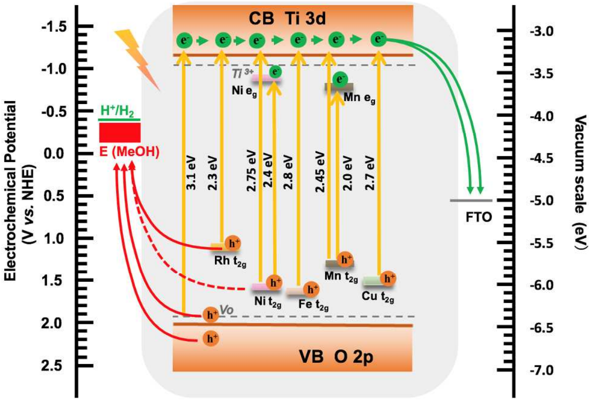

Figure 7. Energy diagram of TM doped SrTiO3 at pH=7. Dopant energy levels are assigned on the basis of the SPS data in Fig. 4. Conduction band (CB) and valence band (VB) edges for $SrTiO_3$ at the point of zero charge were calculated with the Butler-Ginley method,[47] and the FTO work function was taken from the literature.[48]

However, separate work by the Kudo and the Park laboratories has shown that co-doping with La, Nb, or Ta can turn Ni-doped $SrTiO_3$ into a visible light responsive photocatalyst for H_2 and O_2 evolution from sacrificial donors.[10, 12] That emphasizes the importance of co-dopants for creating mobile holes in Ni doped $SrTiO_3$.

CONCLUSION

In summary, we have shown that phase-pure transition metal (Ni, Cu, Fe, Mn, Rh) doped $SrTiO_3$ nanocrystals can be prepared by hydrothermal synthesis from TiO_2, $Sr(OH)_2$, and KOH, in the presence of the transition metal nitrates or chlorides. According to X-ray fluorescence spectroscopy the dopant concentrations are 0.44, 1.24, 1.70, 1.73, 1.05 mol%, respectively, with regard to $SrTiO_3$. The dopants produce mid-bandgap states in the lattice whose energy positions can be estimated by combining data from optical absorption and surface photovoltage spectroscopy. Optical absorption spectra reveal the dopant-induced optical gap, while the photovoltage onset reveals the relative position of the donor states with regard to the conduction band of the $SrTiO_3$ host. Photovoltage size and reversibility provide information on the charge transfer dynamics of the dopants and their ability to trap charge carriers, promote electron-hole recombination, or photooxidize methanol on the nanocrystal surface. Only Rh and to some extent Ni produces states that allow extraction of both electrons and holes, while all other dopants produce states that allow extraction of electrons but not of holes. These findings correlate well with the photocatalytic activity of the nanocrystals: Rh-doped $SrTiO_3$ has the best activity for production of H_2 under visible light, while all other nanocrystals show only minor H_2 evolution with quantum efficiencies of ~0.02% at 435 nm. Overall, this work shows that SPS is a useful tool to assess the energetics and dynamics of electronic states in transition metal doped $SrTiO_3$ nanocrystals. These results will be useful for the design of improved photocatalysts for chemical transformations and solar energy conversion.

EXPERIMENTAL

Strontium hydroxide octahydrate (99%, Alfa Aesar), titanium(IV) oxide (Aeroxide P25, Acros Organics), potassium hydroxide (≥ 85%, Sigma-Aldrich), nickel(II) nitrate hexahydrate (Acros Organics, > 99%), copper(II) nitrate nonahydrate (Acros Organics, 99%), iron(III) chloride hydrate (≥98%, Sigma-Aldrich), manganese chloride (100%, Fisher Scientific), rhodium(III) chloride hydrate (38-41% Rh, Strem Chemicals), dihydrogen hexachloroplatinate(IV) hexahydrate (99.9%, Alfa Aesar), were used as received. Water was purified to 18 MΩ cm resistivity using a Nano-pure system.

$SrTiO_3$ nanocrystals were synthesized following the hydrothermal method reported earlier.[1] 0.598g (2.25 mmol) $Sr(OH)_2{\cdot}8H_2O$, 0.160g P25 TiO_2 (2.00 mmol were used to reduce TiO_2 impurities in the final product), and 1.262g (22.5 mmol) KOH were mixed in 23 mL nanopure water. The solution was transferred to 45 mL PTFE lined autoclave after ultrasonication and stirring for 10 minutes. Then the autoclave was put in an oven and heated at 423 K for 72 hours. After that, the precipitate was washed with diluted hydrochloric acid (to remove $SrCO_3$ and excess $Sr(OH)_2$) and water for five times. Approximately 290 mg of powdered product can be obtained after drying in vacuum overnight, which corresponds to 77% yield based on TiO_2. TM (Ni, Cu, Fe, Mn, Rh) doped $SrTiO_3$ nanoparticles were synthesized in the same way, except that 3mL of a solution containing $Ni(NO_3)_2{\cdot}6H_2O$ (19.6 mg), $Cu(NO_3)_2{\cdot}3H_2O$ (15 mg), $Fe(NO_3)_3{\cdot}9H_2O$ (25.1 mg), $MnCl_2{\cdot}4H_2O$ (12.3 mg), $RhCl_3{\cdot}xH_2O$ (14.1 mg) were added to the reaction mixture. This corresponds to a 3.0 mol% of the TM based on Sr. The samples were denoted as $SrTiO_3$ and M (Ni, Cu, Fe, Mn, Rh): $SrTiO_3$ respectively. A second set of samples for XPS was synthesized by doubling the amount of doping salts to 6.0% mol.

Films for SPS were prepared by drop coating on FTO substrate. In detail, 5 mg/mL aqueous dispersions of the catalysts were ultrasonicated for 3 hours. And FTO glass were cut into pieces and ultrasonicated in acetone, methanol, isopropanol and water for every 20 minutes. Then 0.1 mL of the dispersion was dropped onto pre-cleaned substrates covered with 1×1 cm^2 tape template using a syringe. After drying in air overnight, the films were annealed at 423 K for 2 h.

Modification with Pt. Pt nanoparticles were loaded through a photodeposition method. Typically, 100 mg of photocatalysts were dispersed in 100 mL aqueous methanol (20 vol.%) to which 1.0 mL of the 2.0 mg Pt per mL H_2PtCl_6 (5.18 mg) aqueous solution were added. The solution was stirred and irradiated by a 300 W Xe lamp after evacuated and purged with Ar. After four hours, the powders were centrifuged and washed with pure water seven times and dried in vacuum.

Characterization. Powder XRD scans were performed on Scintag XRD, at a wavelength of $\lambda = 0.154$ nm with 2 mm tube slit divergence, 4 mm scatter, 0.5 mm column scatter and 0.2 mm receiving widths. X-ray fluorescence (XRF) measurements of powder samples were carried out on a Bruker Tiger S8 XRF spectrometer to determine the elemental composition. Rhodium was used as the standard anode material. The tube and generator are designed for a permanent output of 4 kW. XPS measurements were conducted on a Perkin Elmer PHI 5000C ESCA system equipped with Mg Kα radiation. The C1s signal from adventitious carbon at 284.6 eV was chosen as reference. TEM images were recorded on a Philips CM-120 at 80 kV accelerating voltage. Size distribution histograms are obtained by counting 70 crystals in TEM image using Nano Measurer software. UV/vis diffuse reflectance spectra were collected on Thermo Scientific Evolution 220 Spectrometer equipped with integrated sphere. Dried thick films were used for testing by dropping slurry of catalysts on a white filter paper. The reflectance data were converted to the Kubelka-Munk function as $f(R) = (1-R)^2/(2R)$ for scattering correction. For SPS, the sample films were placed into a vacuum chamber and illuminated by monochromatic light from a 150 W Xe lamp filtered through an Oriel Cornerstone 130 monochromator. CPD signals were recorded under vacuum (10^{-5} mBar) and corrected for drift effects by subtracting a dark scan. No adjustment for the variable light intensity of the Xe-light source was made. The thicknesses of the films were measured to be around 3.0 μm by a Dektak 150 profilometer. In the case of films with adsorbed molecules, 0.05 mL of neat methanol (MeOH) were dropped onto the films and allowed to dry at room temperature before subsequent scanning. Transient SPS measurements were conducted at specific wavelength of incident light which is precisely adjusted by the monochromator. Repeated cycles of excitation were achieved by shining and blocking the light source using an equipped shutter.

Photocatalytic tests were conducted on a self-made air-tight irradiation system. The photocatalyst suspension was paced inside of a quartz round-bottom flask and illuminated from the side using a 300 W Xe arc lamp equipped with an IR filter. The intensity at the flask was 600 mW cm^{-2} at λ = 250-680 nm and 20 mW cm^{-2} at λ = 215-355 nm, as determined with GaAsP (SED(SEL005) or SiC UV detectors (SED(SEL270), from International Light, connected to IL1400BL photometer. For visible light studies (<400 nm), the UV portion of the spectrum was removed with a 7.0 cm thick 0.22 M aqueous sodium nitrite solution as filter. The apparent quantum efficiency was measured by conducting the reaction under illumination from a 435 nm monochromatic light emitting diode array (LED 435-66-60, Roithner Lasertechnik). The light intensity measured at reactor was 800 mW cm^{-2} based on a measurement with the GaAsP detector. The reaction system was connected to an online gas chromatograph (Varian 3800) to quantify the amount of gas evolved, using area counts of the recorded peaks. Prior to irradiation, the flask was evacuated and purged with argon gas to 101 kpa.

Conflicts of interest

There are no conflicts to declare.

Acknowledgements

This work was supported by the National Science Foundation (NSF, grant 1464938). X.M. thanks the funding of China Scholarship Council.

Notes and references

1. J. Wang, J. Zhao and F. E. Osterloh, *Energ. Envi. Sci.*, 2015, **8**, 2970-2976.
2. F. E. Osterloh, *Chem. Soc. Rev.*, 2013, **42**, 2294-2320.
3. A. Kudo and Y. Miseki, *Chem. Soc. Rev.*, 2009, **38**, 253-278.
4. M. S. Wrighton, A. B. Ellis, P. T. Wolczanski, D. L. Morse, H. B. Abrahamson and D. S. Ginley, *J. Am. Chem. Soc.*, 1976, **98**, 2774-2779.
5. Y. Ham, T. Hisatomi, Y. Goto, Y. Moriya, Y. Sakata, A. Yamakata, J. Kubota and K. Domen, *J. Mater. Chem. A*, 2016, **4**, 3027.
6. S. Kawasaki, R. Takahashi, K. Akagi, J. Yoshinobu, F. Komori, K. Horiba, H. Kumigashira, K. Iwashina, A. Kudo and M. Lippmaa, *J. Phys. Chem. C*, 2014, **118**, 20222-20228.
7. T. Ohno, T. Tsubota, Y. Nakamura and K. Sayama, *Appl. Catal. A: General*, 2005, **288**, 74-79.
8. E. Grabowska, *Appl. Catal. B: Envir.*, 2016, **186**, 97-126.
9. H. Irie, Y. Maruyama and K. Hashimoto, *J. Phys. Chem. C*, 2007, **111**, 1847-1852.
10. H. W. Kang, S. N. Lim and S. B. Park, *Internat. J. Hydrogen Energy*, 2012, **37**, 10539-10548.
11. F. Li, K. Yu, L.-L. Lou, Z. Su and S. Liu, *Mater. Sci. and Engin.: B*, 2010, **172**, 136-141.
12. R. Niishiro, H. Kato and A. Kudo, *Phys. Chem. Chem. Phys.*, 2005, **7**, 2241.
13. D. Wang, J. Ye, T. Kako and T. Kimura, *J. Phys. Chem. B*, 2006, **110**, 15824-15830.
14. T. Ishii, H. Kato and A. Kudo, *J. Photochem. and Photobio. A: Chemistry*, 2004, **163**, 181-186.
15. Z. B. Jiao, Y. Zhang, T. Chen, Q. S. Dong, G. X. Lu and Y. P. Bi, *Chem. Eur. J.*, 2014, **20**, 2654-2662.
16. K. A. Lehuta and K. R. Kittilstved, *Dalton Trans.*, 2016, **45**, 10034-10041.
17. X. Sun and J. Lin, *J. Phys. Chem. C*, 2009, **113**, 4970-4975.
18. X. Zhou, J. Shi and C. Li, *J. Phys. Chem. C,* 2011, **115**, 8305-8311.
19. R. Konta, T. Ishii, H. Kato and A. Kudo, *J. Phys. Chem. B*, 2004, **108**, 8992-8995.
20. H.-C. Chen, C.-W. Huang, J. C. S. Wu and S.-T. Lin, *J. Phys. Chem. C*, 2012, **116**, 7897-7903.
21. K. Iwashina and A. Kudo, *J. Am. Chem. Soc.*, 2011, **133**, 13272-13275.
22. K. Furuhashi, Q. Jia, A. Kudo and H. Onishi, *J. Phys. Chem. C,* 2013, **117**, 19101-19106.
23. T.-H. Xie, X. Sun and J. Lin, *J. Phys. Chem. C*, 2008, **112**, 9753-9759.
24. K. Tolod, C. Bajamundi, R. de Leon, P. Sreearunothai, R. Khunphonoi and N. Grisdanurak, *Energy Sources, Part A: Recovery, Utilization, and Environmental Effects*, 2016, **38**, 286-294.
25. A. Kubacka, G. Colón and M. Fernández-García, *Catalysis Today*, 2009, **143**, 286-292.
26. Q. Wang, T. Hisatomi, Q. Jia, H. Tokudome, M. Zhong, C. Wang, Z. Pan, T. Takata, M. Nakabayashi, N. Shibata, Y. Li, I. D. Sharp, A. Kudo, T. Yamada and K. Domen, *Nature Mater.*, 2016, **15**, 611-615.
27. B. Kiss, T. D. Manning, D. Hesp, C. Didier, A. Taylor, D. M. Pickup, A. V. Chadwick, H. E. Allison, V. R. Dhanak and J. B. Claridge, *App. Catal. B: Envir.*, 2017, **206**, 547-555.
28. A. Kudo, R. Niishiro, A. Iwase and H. Kato, *Chemical Physics*, 2007, **339**, 104-110.
29. D. Cuong do, B. Lee, K. M. Choi, H. S. Ahn, S. Han and J. Lee, *Phys. Rev. Lett.*, 2007, **98**, 115503.
30. R. Merkle and J. Maier, *Phys. Chem. Chem. Phys.*, 2003, **5**, 2297-2303.
31. W. Choi, A. Termin and M. R. Hoffmann, *J. Phys. Chem. C.*, 1994, **98**, 13669-13679.

32. K. Mizushima, M. Tanaka, A. Asai, S. Iida and J. B. Goodenough, *J. Phys. Chem. Solids*, 1979, **40**, 1129-1140.
33. L. Kronik and Y. Shapira, *Surf. Sci. Rep.*, 1999, **37**, 1-206.
34. J. Zhao and F. E. Osterloh, *J. Phys. Chem. Lett*, 2014, **5**, 782–786.
35. Y. Yang, J. Wang, J. Zhao, B. A. Nail, X. Yuan, Y. Guo and F. E. Osterloh, *ACS Appl. Mater. & Interf.*, 2015, **7**, 5959-5964.
36. T. L. Shelton, N. Harvey, J. Wang and F. E. Osterloh, *Appl. Catal. A: General*, 2015.
37. P. Wu, J. Wang, J. Zhao, L. Guo and F. E. Osterloh, *J. Mater. Chem. A*, 2014, **2**, 20338-20344.
38. J. Lagowski, P. Edelman, A. M. Kontkiewicz, O. Milic, W. Henley, M. Dexter, L. Jastrzebski and A. M. Hoff, *Appl. Phys. Lett.*, 1993, **63**, 3043-3045.
39. B. Wang, Y. Wang, L. Fan, Y. Cai, C. Xia, Y. Liu, R. Raza, P. A. van Aken, H. Wang and B. zhu, *J. Mater. Chem. A*, 2016, **4**, 15426-15436.
40. A. Yamakata, M. Kawaguchi, R. Murachi, M. Okawa and I. Kamiya, *J. Phys. Chem. C*, 2016, **120**, 7997-8004.
41. R. Konta, T. Ishii, H. Kato and A. Kudo, *J. Phys. Chem. B*, 2004, **108**, 8992-8995.
42. Y. Sasaki, H. Nemoto, K. Saito and A. Kudo, *J. Phys. Chem. C*, 2009, **113**, 17536-17542.
43. H. Tan, Z. Zhao, W. B. Zhu, E. N. Coker, B. Li, M. Zheng, W. Yu, H. Fan and Z. Sun, *ACS Appl. Mater. & Interf.*, 2014, **6**, 19184-19190.
44. J. Nowotny, M. A. Alim, T. Bak, M. A. Idris, M. Ionescu, K. Prince, M. Z. Sahdan, K. Sopian, M. A. M. Teridi and W. Sigmund, *Chem. Soc. Rev.*, 2015, **44**, 8424-8442.
45. D. J. Lam, B. W. Veal and D. E. Ellis, *Phys. Rev. B*, 1980, **22**, 5730-5739.
46. T. Mizokawa and A. Fujimori, *Physical Review B*, 1995, **51**, 12880-12883.
47. M. Butler and D. Ginley, *J. Electrochem. Soc.*, 1978, **125**, 228-232.
48. D. R. Lide, *CRC Handbook of chemistry and physics*, CRC press, 2004.